

Supplementary Methods

Stimuli and Task

We trained 6 adult macaque monkeys (S, E, R, B, J and C) to perform the texture segregation task. A trial began with the fixation point (a red circle of 0.3° diameter) presented on a grey background and the monkey began the trial by directing gaze to a one degree fixation window centred on the fixation point. After 300ms of fixation the texture stimulus was presented. After a further 300ms, the fixation circle was extinguished and the monkey was required to make a saccadic eye-movement into a target-window (4 degrees diameter) centered on the figure position. Correct responses were rewarded with apple juice. Trials in which the animal broke fixation before the fixation point was extinguished were aborted. On 25% of trials we presented a homogeneous texture without a figure (catch condition) and the animals were rewarded for carrying on fixating within the fixation window for a further 400ms. All stimulus conditions were presented in a pseudorandom order.

All stimuli were generated using in-house software and were presented on a CRT monitor with a resolution of 1024x768 pixels and refresh rate of 85Hz, which was viewed from a distance of 75cm. The figure-ground stimuli were full-screen bitmaps of textures consisting of black oriented line elements (45 and 135 orientation) on a white background. Two bitmaps of each texture orientation (i.e. two leftwards oriented and two rightwards oriented textures) were made with randomly placed elements (5345 elements per bitmap with a thickness of 1 pixel and a length of 16 pixels). To make the figure stimuli, a square region of one bitmap of 4 x 4 degrees with the center located on the RF was copied onto the same position of a full-screen bitmap of the orthogonal orientation. Four different versions of each stimulus were made by combining each texture with a figure from one of the two orthogonal textures. These four texture-

combinations were shown in a counter-balanced order, ensuring that on average precisely the same contour elements were present inside the RF across the different conditions. Two background conditions were created by rotating the location of the figure 120 or 240 degrees around the fixation point.

Surgical procedures

The animals underwent two surgeries under general anesthesia that was induced with ketamine (15mg/kg injected intramuscularly) and maintained after intubation by ventilation with a mixture of 70% N₂O and 30% O₂, supplemented with 0.8% isoflurane, fentanyl (0.005mg/kg intravenously) and midazolam (0.5mg/kg/h intravenously). In the first operation a head holder was implanted and in monkeys S, E, B, J and C a gold ring was inserted under the conjunctiva of one eye for the measurement of eye position (we measured the eye position of monkey R with a camera system). The monkeys were then trained until they could reliably perform the task. In monkeys S, E and R a recording chamber (Crist Instruments) was subsequently implanted over the operculum of V1 and a craniotomy was performed inside the chamber for the laminar recordings. In monkeys B, J and C multiple grids of 4x5 microelectrodes with 1-1.5 mm length needles (Cyberkinetics Neurotechnology Systems Inc.) were chronically implanted in areas V1 and V4. The 1 mm electrode tips are likely to end up in layer 4 and the 1.5mm tips in layer 4 or just below in layer 5. All procedures complied with the NIH Guide for Care and Use of Laboratory Animals (National Institutes of Health, Bethesda, Maryland), and were approved by the institutional animal care and use committee of the Royal Netherlands Academy of Arts and Sciences.

Data acquisition and preprocessing

Neuronal data was collected with TDT (Tucker Davis Technology) recording equipment using a high-impedance headstage (RA16AC) and a preamplifier (either RA16SD or PZ2) with a high-pass filter of 2.2Hz, a low-pass filter of 7.5 kHz (-3dB point) and sampled with a rate of 24.4kHz. As in previous studies (1-3), the digitized signals were band-pass filtered (500Hz-5kHz), full-wave rectified and low-pass filtered (200Hz) to produce an envelope of the multi-unit activity (MUA). This MUA signal provides an average of spiking activity of a number of neurons in the vicinity of the tip of the electrode and the population response obtained with this method is therefore expected to be identical to the population response obtained by pooling across single units (4). For the spectral properties of neuronal activity, MUA gives a higher signal-to-noise ratio than single unit data (1, 5). We applied a low-pass filter (<200Hz) to record the local field potential (LFP).

We used multi-contact ‘U’ probes (Plexon) for the laminar recordings with 24 contact points spaced 100 μ m apart (Fig. 1B). Either the metal shaft of the probe or a silver/silver chloride wire in the recording chamber served as reference. We lowered the electrode across the dura with a micro-manipulator (Narishige, Japan) at a relatively fast rate (\sim 100 μ m/s) to minimize dimpling of the cortex and ascertained when the first contact point passed the dura by careful visual inspection of the LFP and we then reduced the speed to \sim 10 μ m/s.

We calculated the one-dimensional current source density (CSD) from the LFP following Mitzdorf (6) as:

$$CSD(x) = -\sigma \cdot \frac{\phi(x-h) - 2\phi(x) + \phi(x+h)}{h^2}$$

Where ϕ is the voltage, x is the point at which the CSD is calculated, h is the spacing of electrodes for the computation (here we used a spacing of 200 μ m) and σ is the conductivity of cortical tissue (we used a value of 0.4S.m⁻¹) (7). The CSD is a measure of the currents flowing towards or away from electrode contact points (8, 9).

To determine the depth of the electrode we measured the CSD evoked by a full-screen 100% contrast checkerboard (presented for 250ms while the monkey fixated, check size 0.3°) (6, 10). We estimated the location of the border between layer 5 and layer 4C as the polarity reversal from current sinks in layer 4C to current sources in the deep layers around 40ms after stimulus onset (8, 10) (Fig. S1). We placed the electrode so that the CSD reversal was as close as possible to the 8th contact from the tip to ensure coverage of all cortical layers. We estimated the position of the other layers on the basis of histological data (11, 12). We mapped the receptive fields (RFs) of every recording site of the electrode (see below for the RF mapping methods). When the RFs of the recording sites in different layers did not overlap, indicating that the probe was not perpendicular to the cortical surface, the probe was retracted and inserted at a different location. In the final analysis we aligned the data from different penetrations using the CSD reversal of the visual response evoked by the figure-ground stimuli. We removed line noise by fitting a 50Hz sinusoid to the LFP signal of each trial and subtracting it. We calculated the signal-to-noise-ratios (SNR) of every MUA recording site as the height of the peak of the stimulus-evoked response divided by the standard deviation of activity in the prestimulus period. Only recording sites with an SNR>3 were included in the analysis.

In monkeys B and J recordings were made with microelectrode grids in V1 and V4 with overlapping receptive fields (Fig. S17). To measure the local V1 and V4 LFP for the power and coherence analysis, we referenced the LFP to an electrode within the same array. Hardware filters in the preamplifier stage induce phase shifts in the signal (13). We measured the shift for every frequency and corrected for them in the frequency domain.

Eye movements were recorded either with a scleral search coil using the double-induction technique (14) and sampled at 1017Hz, or using a video eye-tracker (Thomas recordings) with a sampling rate of 350Hz.

Electrical microstimulation

We carried out electrical microstimulation experiments in monkeys B and C using the microelectrode grids in V1 and V4. We delivered trains of 5 biphasic pulses of 500 μ s duration (250 μ s per phase) at a frequency of 200Hz with an amplitude in the range of 30-100 μ A using a custom-made constant current stimulator. In the first phase of the pulse, one electrode of the V1 or V4 array served as cathode and another electrode in the same array as anode and the polarity was reversed in the second phase. An advantage of this stimulation configuration is that it reduced the stimulation artifact in the other area where we recorded the LFP.

Drug injections

Some of the laminar probes contained a fine glass capillary tube for the injection of fluids into the cortex. The exit point of the tube was commonly between contacts points 7 and 8. The tubes were filled using polyethylene tubing and Hamilton syringes (1 μ L). Drugs were dissolved either in filtered water or artificial cerebrospinal fluid. The drug was filtered using a sterile microfilter (Millipore, 0.23 μ m filter). All drugs were obtained from Sigma and were used in the following

concentrations: 50 mM APV, 5–10 mM CNQX, and 50–100 μ M ifenprodil. We used pressure injection to administer small volumes (25–80 nL) with a Hamilton syringe, either in 10nL steps or in a larger bolus.

Receptive field mapping

We measured the V1 receptive field dimensions by determining the onset and offset of the response to a slowly moving light bar for each of eight movement directions (15). The MUA RF size in V1 was 1.2 deg on average (standard deviation = 0.28 deg) and the eccentricity was between 1.8 and 5.5 deg (median = 3.7 deg). We mapped the V4 RFs by presenting white dots (0.5-1 deg diameter, luminance 82cd/m²) on a grey background (luminance 14cd/m²) at different positions of a grid (0.5 deg spacing). We defined the RF borders as the locations where activity fell below 50% of the maximum (16). With this definition, the median V4 RF area was 13.6 deg² (range 6.5 to 37.7 deg²). RFs in V4 were considerably larger than those in V1 but there was substantial overlap (Fig. S17). In the figure condition of the task the V1 RFs fell in the center of the figure.

Data analysis and statistics

Figure 2A shows the MUA population response evoked by the figure and the background. Before pooling responses across the individual MUA recording sites we normalized their activity by subtracting the average spontaneous activity in a window of 150ms before stimulus onset and then dividing by the peak response in the background condition.

We used wavelet analysis and correlation analysis to calculate spectral estimates (17). The Fourier transform of the signal $x^r(t)$ of every recording site j and every trial r was

calculated and convolved with a set of complex Morlet-filters to obtain the time- and frequency-dependent spectrum:

$$F_j^r(t, \omega) = \int dt' g(t, t', \lambda_c, \lambda_b) x_j^r(t')$$

With the complex Morlet filters given by:

$$g(t, t', \lambda_c, \lambda_b) = \frac{1}{\lambda_b \sqrt{\pi}} e^{-\frac{(t-t')^2}{\lambda_b^2}} e^{-i \frac{(t-t')}{\lambda_c}} \text{ with } \lambda_c = 2\pi / \omega \text{ and } \lambda_b = \alpha \lambda_c.$$

This can be understood as a complex exponential with wavelength λ_c , windowed by a Gaussian with a standard deviation equal to $\lambda_b / \sqrt{2}$. λ_b is set equal to λ_c times the scaling parameter α , making the length of the wavelet linearly dependent on the frequency. α was set to 1, making the standard deviation of the wavelet envelope equal to $\lambda_c / \sqrt{2}$. The effective temporal bandwidths of the wavelets therefore corresponded to $100 / \sqrt{2}$ ms for alpha and about $17 / \sqrt{2}$ ms for gamma. The time representation of the wavelet envelopes were truncated at $\pm 3\lambda_b$. The wavelet envelopes were allowed to extend beyond the chosen time window by maximally half a Gaussian.

The power spectrum of site j was defined as:

$$P_j(t, \omega) = \frac{1}{N} \sum_{r=1}^N |F_j^r(t, \omega)|$$

where N is the total number of trials (18). The cross spectral density function for recording sites j and k was calculated for each trial r as:

$$S_{jk}^r(t, \omega) = \frac{1}{T} F_j^r(t, \omega)^* F_k^r(t, \omega)$$

where the $*$ denotes the complex conjugate. This equation can also be expressed as:

$$S_{jk}^r(t, \omega) = C_{jk}^r(t, \omega) - iQ_{jk}^r(t, \omega)$$

where the real part, denoted by $C_{jk}^r(t, \omega)$, is the coincidence spectral density function and the imaginary part $Q_{jk}^r(t, \omega)$ is the quadrature spectral density function. The coherence function was calculated from the cross spectral density as:

$$Coh_{jk}(t, \omega) = \frac{\left| \sum_{r=1}^N S_{jk}^r(t, \omega) \right|}{\sqrt{\sum_{r=1}^N S_{jj}^r(t, \omega) \sum_{r=1}^N S_{kk}^r(t, \omega)}}$$

and the instantaneous phase function as:

$$Ph_{jk}(t, \omega) = -\tan^{-1} \frac{\sum_{r=1}^N Q_{jk}^r(t, \omega)}{\sum_{r=1}^N C_{jk}^r(t, \omega)}$$

To compute the LFP-MUA and CSD-CSD coherence, we selected sites on the laminar probe with a distance of 200 μ m.

The analysis window was from 150 to 350ms after the presentation of the visual stimulus (unless otherwise noted). For these analyses the average LFP signal over all trials was subtracted from the signal of every trial, separately for each condition and each channel to focus on internally generated rhythms. To estimate the contribution of stimulus locked activity to the coherence measurements we repeated the analysis for shuffled trials but observed no clear peaks (dashed lines in Fig. S3), which confirmed that oscillatory activity was not time-locked to the stimulus onset (see also Fig. 2B, 6D, S19A,B). Furthermore, the effects of the task on the LFP power and LFP-MUA did not critically depend on the subtraction of the stimulus-evoked LFP

potential (Fig. S19C-F) as they occurred in a time-window after the strongest components of the evoked potential.

We carried out permutation tests to determine the p-values for differences in LFP power between conditions, separately for low frequencies (below 25Hz) and high frequencies (above 30Hz) (Fig. S2A-C). Specifically, we shuffled the class labels (figure or ground) 10,000 times and determined the mean power spectrum across recording sites, calculated the difference spectrum for each permutation and stored only the highest and lowest differences in power. This resulted in a distribution of 20,000 values from which p-values could be determined by calculating the upper and lower percentiles corresponding to that p-value (for example the 0.05 and 99.95 percentiles for a p-value of 0.001) (19). CircStat, a toolbox for circular statistics, was used for all statistical analyses involving phases (20).

Because oscillatory activity is not necessarily linked to external events that can serve as triggers to average individual waves of activity, we used the troughs of oscillatory activity in the LFP as reference points (21, 22). To select genuine oscillatory activity, we selected the 50% of trials with highest power in the relevant frequency band (we obtained equivalent results if we included all trials). We determined the troughs by filtering the LFP of one recording site in layer 4C (~250 μ m above the CSD reversal between layer 4C and layer 5) in the desired frequency band (8-12Hz for alpha and 55-65Hz for gamma) (Fig. S6). Only troughs occurring in a period from 150-350ms after stimulus onset were stored, after which the filtered signal was not used further. Time windows around the troughs were then used to average the LFP, the CSD and the MUA of all channels, after subtraction of the mean response (equivalent to subtraction of the shift-predictor). The size of these time windows was 1.5 times the period of the mean filtered frequency, and we excluded windows that extended beyond 100-350ms after stimulus onset. All

trough-triggered traces were added together, divided by the total number of troughs per monkey and subsequently averaged across monkeys. We expressed the amplitude of the fluctuations in the MUA revealed by this analysis (Fig. 3) as fraction of the mean MUA response in the window from 150-350ms after stimulus onset, after smoothing with a sliding window of 5ms for gamma and 25ms for alpha.

To measure the phase shifts in MUA between layers, we averaged LFP-triggered MUA across laminar compartments (Fig. 3D,H). We assigned recording sites between 550 and 50 μ m below the CSD reversal to the deep layers, between 50 and 550 μ m above the reversal to layer 4, and between 650 and 1050 μ m above the reversal to the superficial layers. To estimate phase differences between the MUA in different compartments we fitted a sinusoid with the frequency of the band-pass filter used to determine the LFP troughs. Statistical significance of these time delays was calculated over penetrations (i.e. recording days). We extended this analysis by determining LFP-troughs for a wide range of frequencies (in steps of 2 Hz using a band-pass filter with a width of 4Hz, i.e. 2Hz overlap between adjacent frequency bins) to investigate how the MUA phase differences between laminar compartments depend on frequency (Fig. S7).

We used the MVGC toolbox (23) to compute Granger causality with a model order of 50ms (24, 25). We used the CSD to compute the Granger causality between layers and the bipolar LFP for Granger causality between V1 to V4. We used bootstrapping to estimate the s.e.m. (10.000 samples) and permutation tests to calculate the significance of the difference in Granger causality between layers and between V1 and V4 averaged in the alpha and gamma band (10.000 permutations). We controlled for multiple comparisons between layers by calculating for each permutation the full matrix of comparisons between laminar compartments averages within the alpha and gamma band. Of each permutation only the maximum and

minimum value was taken within this matrix. This resulted in a distribution of 20.000 values from which we determined the p-values (the 0.05 and 99.95 percentiles for a p-value of 0.001).

Design of anatomical figures

For the lateral view of the macaque brain in Fig. 1A we adapted drawings of Nieuwenhuis et al. (26) and Krieg (27). The Nissl section illustrating the different layers in Figs. 1B and S18A was adapted from O'Kusky and Colonnier (12).

Supplementary Results

Catch trials

Figure S5H compares the MUA response elicited by a homogeneous background (the catch condition, Fig. S5C) to the response elicited in the background condition with a figure far from the RF (the ground condition, Fig. S5B). The presence of a figure outside the neurons' RF caused a slight additional suppression of the MUA response (time window from 200-30ms after stimulus onset, t-test, $P < 0.001$). Similarly, the gamma LFP-MUA coherence was slightly lower if the neurons' receptive field fell on the background than in the catch condition (Fig. S5E). Both effects are presumably caused by the selection of a figure outside the RF in the ground condition, and are in accordance with the finding that attentional selection increases the MUA responses as well as gamma oscillations (Fig. 2A,D). The LFP power in the alpha band was somewhat higher in the ground than in the catch condition, but effect did not occur for the LFP-MUA coherence.

Granger causality

Figure S15 illustrates the full multivariate Granger causality frequency spectrum between layers. Causality that is directed upwards (towards the pia) is plotted in red and downwards in blue. For the low frequencies, Granger causality was directed from the deep layers towards layer 4 (note that the largest low frequencies peaks are red) and also from the superficial layers towards layer 4 with a remarkably narrow peak, which was consistently located at 10Hz. This finding supports the hypothesis that the deep and very superficial layers influence activity in the middle layers, and is in accordance with the profile of phase differences between these layers for the alpha rhythm (Fig. 3) and also with the coherence analysis (Fig. S13). In contrast, the peak in the Granger causality analysis in the gamma range revealed directional influences from layer 4AB to

layer 3 and, in addition, a directional influence from layer 4C and layer 6 towards layer 5. This profile therefore matches the laminar profile of phase differences evident in the trough triggering analysis (Fig. 3) and in the coherence analysis across layers (Fig. S13). A previous study also investigated Granger causality across layers in monkey V1 (25). We notice that the electrodes used in the present study allowed a more fine-grained analysis of the CSD patterns due to the smaller spacing between electrodes (100um as opposed by 150um in ref. 25). We confirm some of the previous findings, but also obtained important additional insights. First, we found that the strongest generator in the alpha range was in the deep layers, in line with the results from Bollimunta et al. (24, 25). Second, we also observed a generator in the very superficial layers driving downwards. Third, we found that the generator of the alpha was in layer 5/6, not in layer 4 as reported by Bollimunta et al (25). This result is in line with our analysis of the CSD-MUA coherence, which demonstrated that MUA locking to the alpha rhythm coincided with a sink in layer 5 (Fig. 3B,C). A possibility explanation for the discrepancies between the studies is provided by the improved spatial resolution provided by the narrower spacing between the contact points of our laminar probes, which also enabled a better localization of the boundary between layers 4c and 5 and thereby a more accurate alignment of different penetrations.

Supplementary Figures

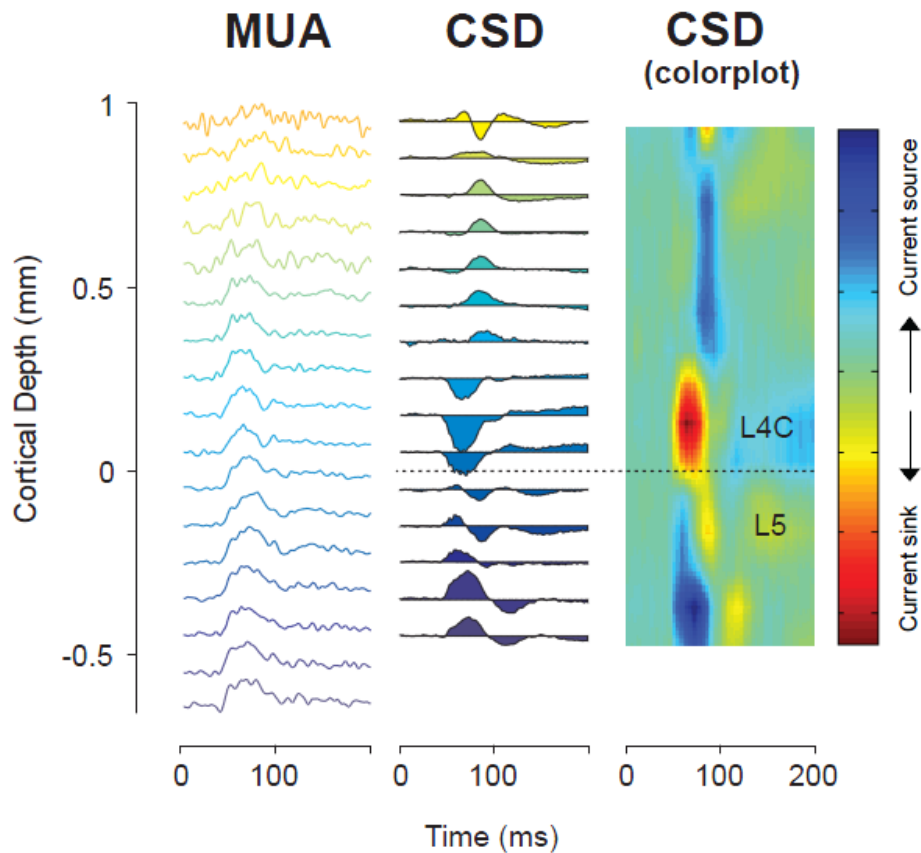


Fig. S1. Example of laminar recordings. An example penetration showing the MUA (left graph) and CSD (middle and right graph) triggered by a full-screen, full-contrast checkerboard stimulus. Simultaneous responses from 17 contacts are shown stacked. In the leftmost columns blue colours indicate deeper channels and green/yellow colours indicate shallow channels. MUA was normalized to the peak of the response for each recording site. In the right column the red colours show current sinks and the blue colours current sources. The dashed line shows the boundary between layers 4 and 5, estimated as the transition between the earliest sink and source evoked by the appearance of the visual stimulus.

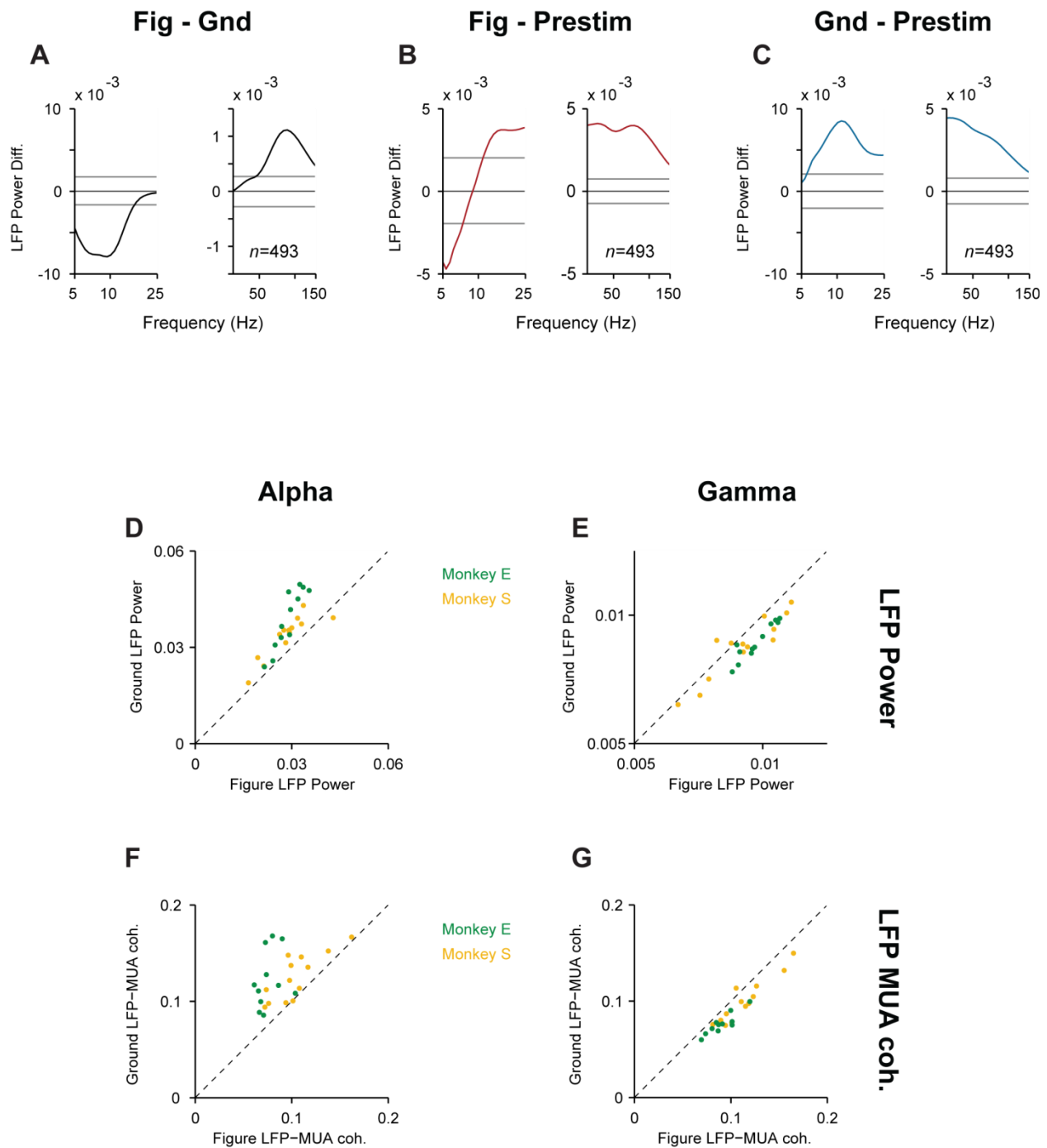


Fig. S2. Supplementary statistics for LFP power and LFP-MUA coherence. (A) Difference in LFP power between the response evoked by the figure and the background in a window from 150-350ms after stimulus onset. (B) Difference in LFP power between the response evoked by

the figure and the pre-stimulus period (200-0ms before stimulus onset). (C) Difference in LFP power between the response evoked by the background and the pre-stimulus period. Grey lines indicate $p < 0.001$ (signed permutation test; $n = 493$ recording sites). (D-G) Scatter plots for LFP power (D,E) and LFP-MUA coherence (F,G) for the alpha (D,F) and gamma band (E,G) elicited by the figure (abscissa) and background (ordinate). Yellow circles indicate penetrations for monkey S (13 penetrations) and green circles for monkey E (11 penetrations) (t -test, $P_S < 0.001$ for all comparisons).

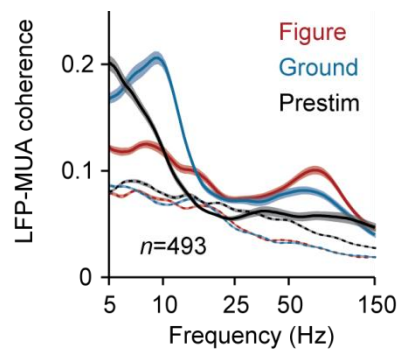


Fig. S3. Average LFP-MUA coherence in the figure (red trace) and background condition (blue trace) during the modulation period, and the pre-stimulus period (black trace). The dashed lines indicate the LFP-MUA coherence for shuffled trials. Notice that these spectra fell below the unshuffled trials and showed no clear peaks, indicating that oscillatory activity was significant and not time-locked to the stimulus onset. Shaded areas show s.e.m. in all plots ($n=493$ recording sites), when they are difficult to see the s.e.m. is small.

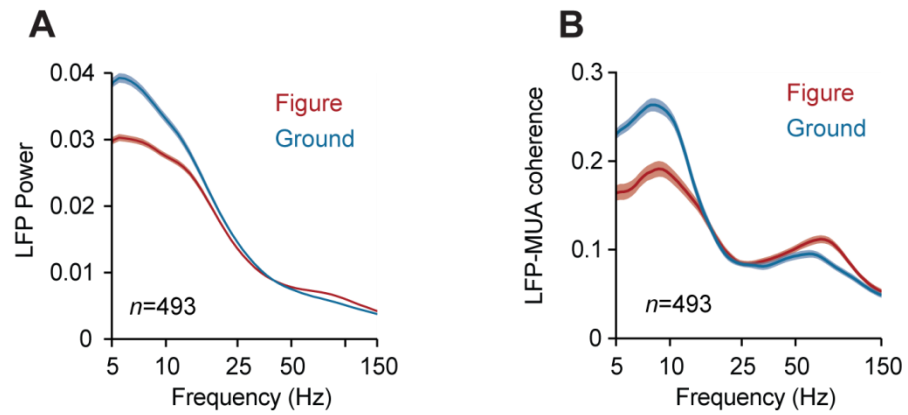


Fig S4. Control analysis with extended time-window. LFP power spectrum (A) and LFP-MUA coherence (B) in a window from 150-450ms in trials with a reaction time longer than 420ms, for the figure (red trace) and ground condition (blue trace).

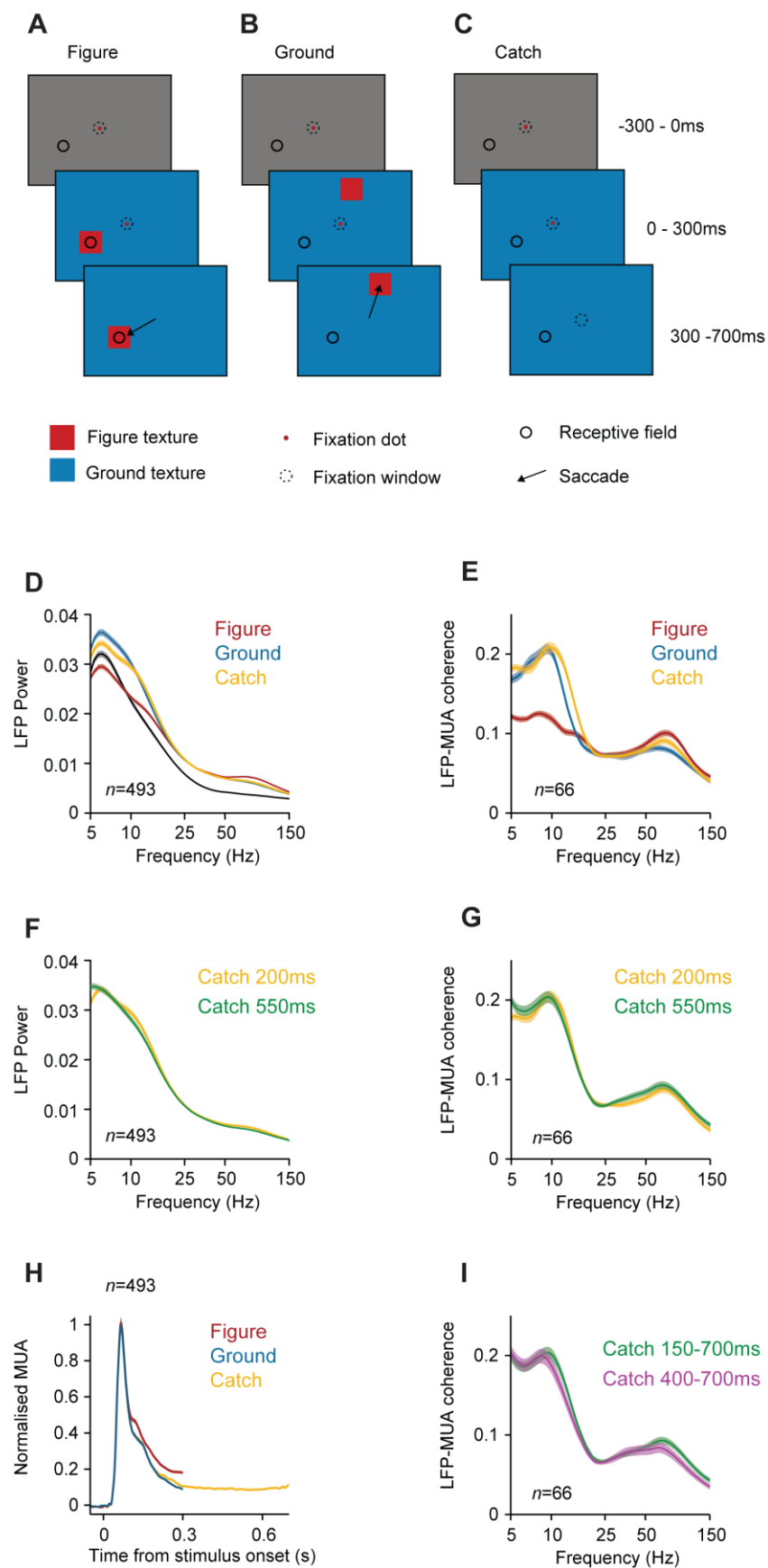


Fig. S5. Power spectra and LFP-MUA coherence in catch trials. Schematic representation of the time course of the task and the different trial types. The monkeys started a trial by fixating within a small window (indicated by the dashed circle) centered on a fixation point (indicated by the red dot). After 300ms, a figure-ground texture appeared (the blue region illustrates the background, the red square illustrates the location of the figure). (A-C) In the figure condition (A), a figure was centered on the neurons' receptive field (circle) and in the ground conditions (B) the figure appeared at one of two other locations so that the receptive field fell on the background. The monkeys were rewarded for an eye movement to the figure (arrow). There were also 25% catch trials with a homogenous texture of one orientation. The monkey was rewarded for maintaining fixation for another 400ms (C), so that we could analyze the power spectrum in a longer time window. (D,E) LFP power spectrum (D) and LFP-MUA coherence (E) for the figure condition (red trace), the ground condition (blue trace) and the catch condition (yellow trace), in a time window from 150-350ms after stimulus onset. (F, G) Comparison of the LFP power (F) and LFP-MUA coherence (G) in the catch condition in a 200ms (150-350ms after stimulus onset, yellow trace) and a 550ms time-window (150-700ms after stimulus onset, green trace). Shaded areas show s.e.m. in all plots ($n=493$ recording sites). (H) Average MUA response in V1 evoked by the figure (red trace), the background (blue trace) and the catch condition ($n=493$ recording sites). The traces for the figure and ground condition are truncated at the time when the monkey was allowed to make a saccade. Note that the MUA in catch trials reaches a relatively stable level in the later period of the trial. (I) Average LFP-MUA coherence in the catch condition in a window from 150-700ms after stimulus onset (green) and 400-700ms after stimulus onset (purple). Shaded areas show s.e.m. in all plots ($n=493$ recording sites).

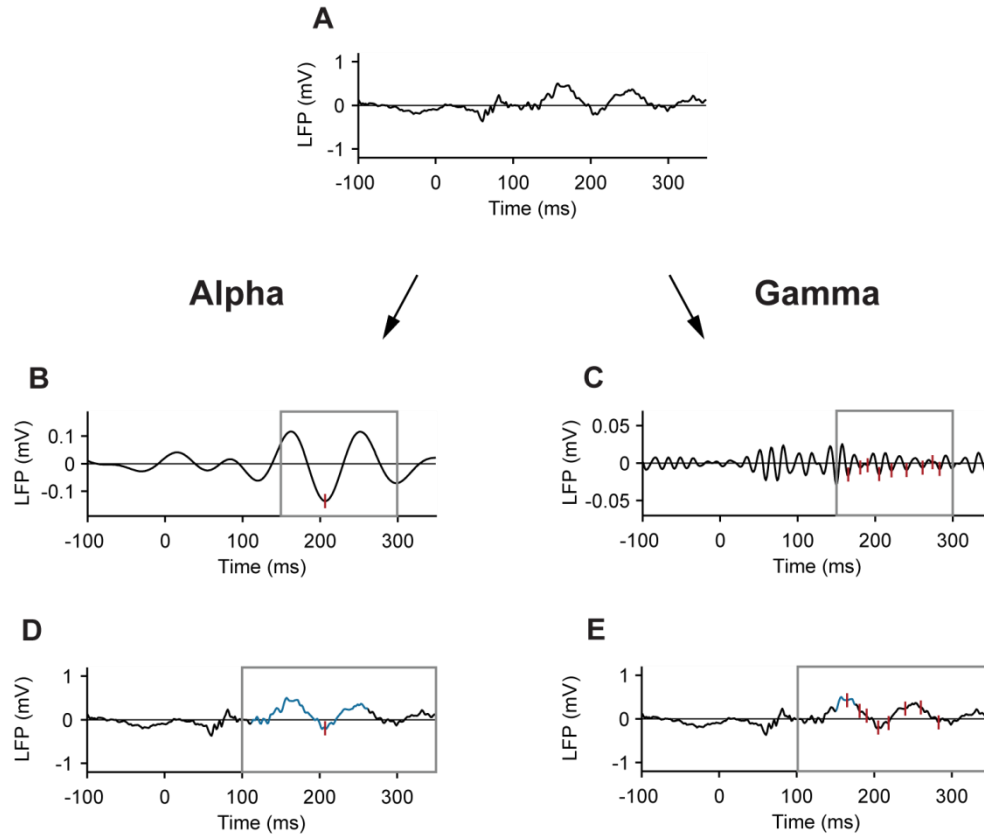


Fig. S6. Trough-triggering analysis. (A) LFP trace of a representative trial where the RF of a recording site fell on the background, after subtraction of the mean evoked potential. Note the presence of alpha and gamma oscillations. (B,C) To determine the timing of troughs of the oscillations, the LFP was filtered between 8-12Hz (B) and 55-65Hz (C). Red marks indicate troughs within the computational window (150-300ms, grey rectangle). (D,E) The troughs detected in the filtered signal were mapped back onto the broad-band LFP for averaging.

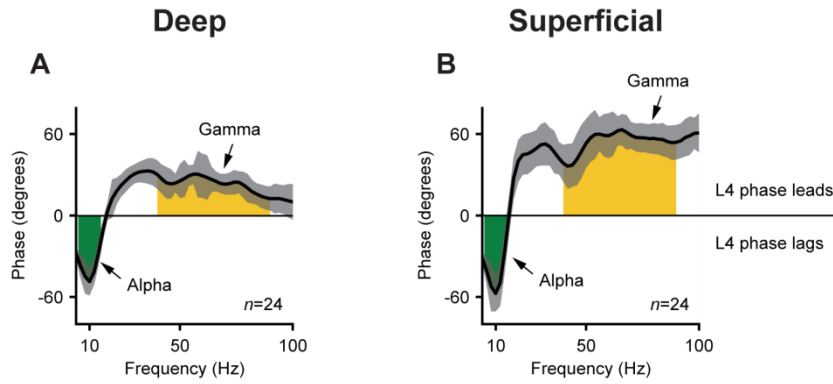


Fig. S7. MUA phase in deep and superficial layers relative to layer 4. MUA phase in the deep (A) and superficial layers (B) relative to the MUA in layer 4 for different frequencies. We aligned the MUA on the troughs of the LFP in layer 4 for different frequencies with a band-pass filter (width of 4Hz). Positive values denote a phase lead of layer 4. Green and yellow areas indicate the frequencies that we assigned to the alpha (5-15Hz) and gamma (40-90Hz) range. Shaded areas show s.e.m. ($n=24$ penetrations).

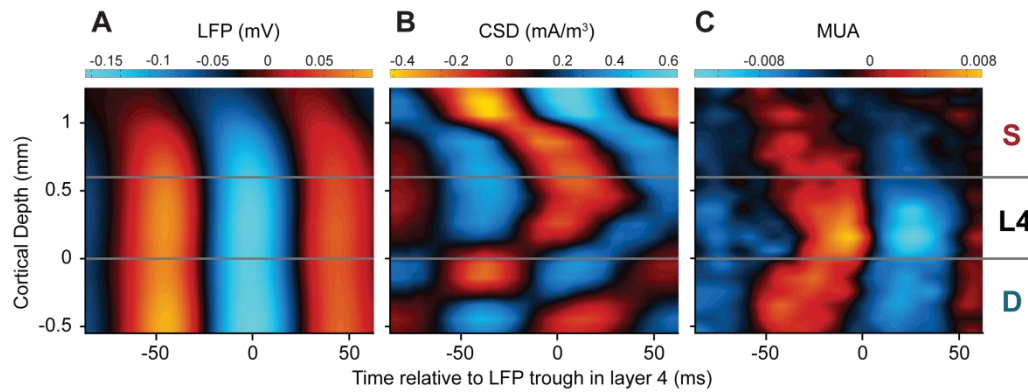


Fig. S8. Laminar profile of alpha oscillations in the prestimulus period. (A) Laminar profile of the LFP (mV) relative to the alpha troughs in a window from 150-0ms before stimulus onset, averaged across 24 penetrations. Negative potentials are shown in blue, positive potentials in red. (B) Average laminar profile of the CSD (mA/m³) relative to LFP troughs in layer 4 for the alpha rhythm. Current sinks are shown in red, sources in blue. (C) MUA aligned to the LFP troughs in layer 4. Red colors show MUA that is higher than the average and blue colors MUA lower than the average.

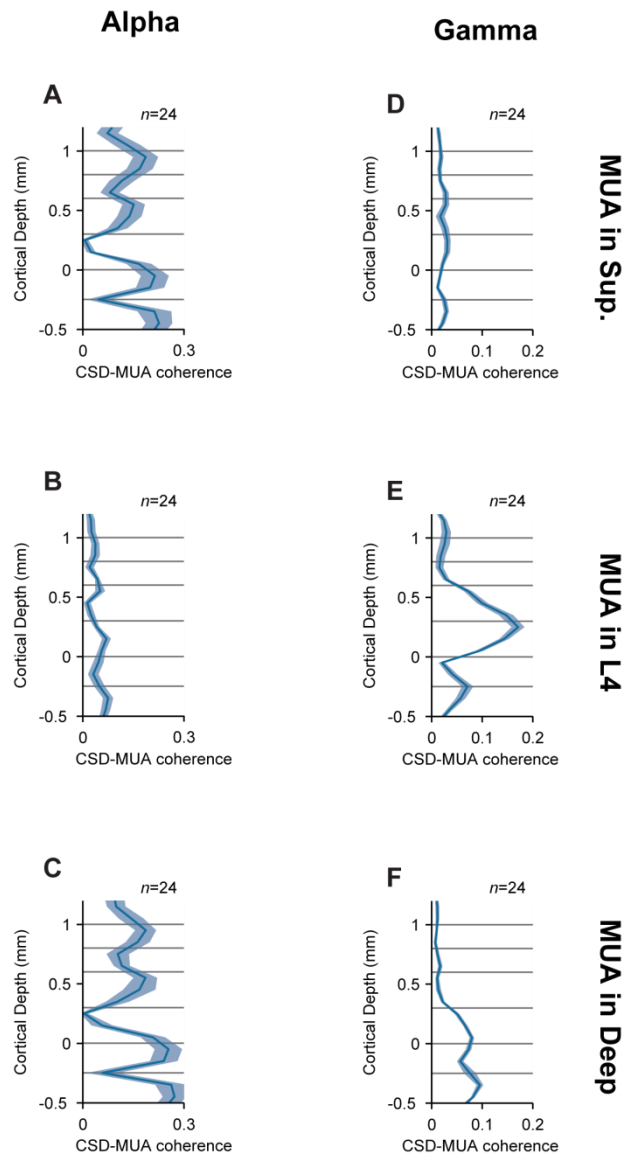


Fig. S9. Laminar profile of CSD-MUA coherence for the alpha band (A-C) and the gamma band (D-F) separately for the MUA averaged across superficial layers (A,D), layer 4 (B,E) and deep layers (C,F).

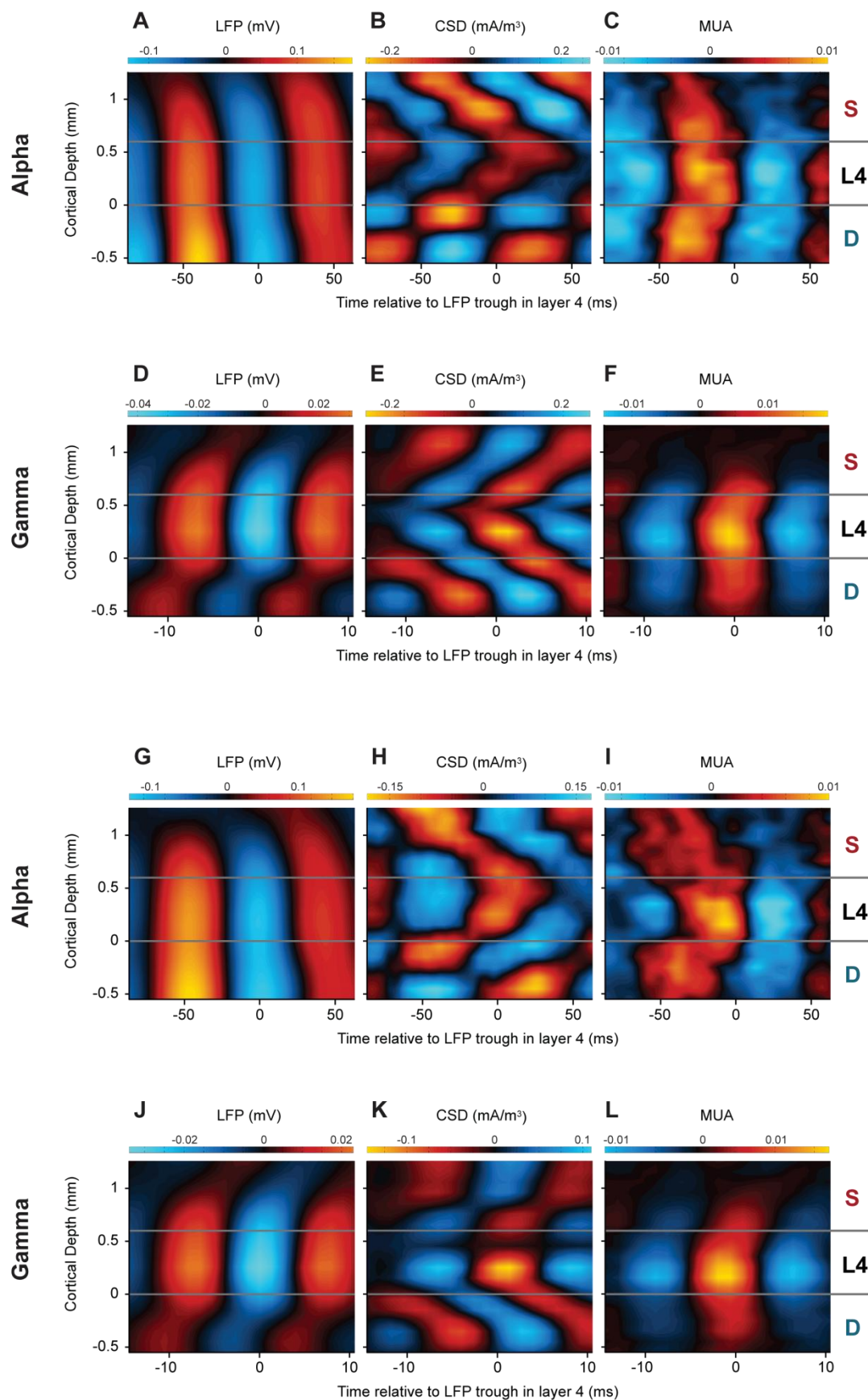
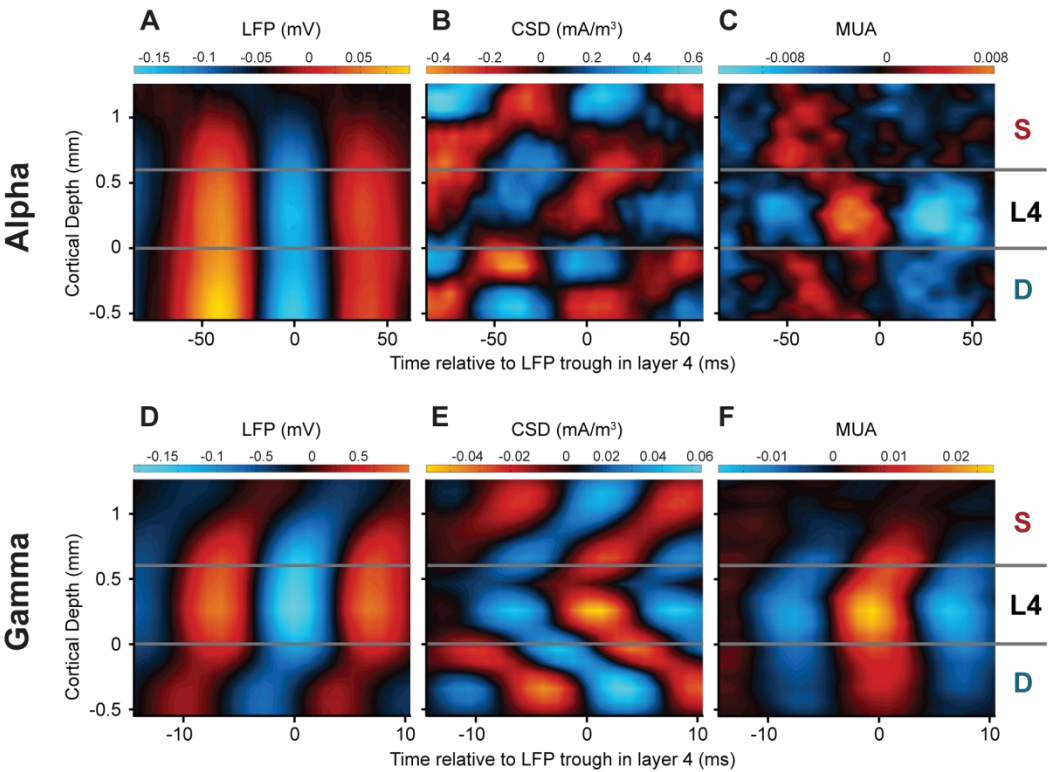


Fig. S10. Laminar profile of cortical oscillations separately for monkey E (A-F) and monkey S (G-L). (A) Laminar profile of the LFP (mV) relative to the alpha troughs in a window from 150-300ms after stimulus onset, averaged across 11 penetrations of monkey E. Negative potentials are shown in blue, positive potentials in red. (B) Average laminar profile of the CSD (mA/m³) relative to LFP troughs in layer 4 for the alpha rhythm. Current sinks are shown in red, sources in blue. (C) MUA aligned to the LFP troughs in layer 4. Red colors show MUA that is higher than the average and blue colors MUA lower than the average. (D-F) Same analysis as in A-C, but now the data was aligned to the troughs of the gamma rhythm (55-65Hz) in layer 4. (G-L) Same analysis as in A-F but averaged across 13 penetration for monkey S.

Figure



Catch

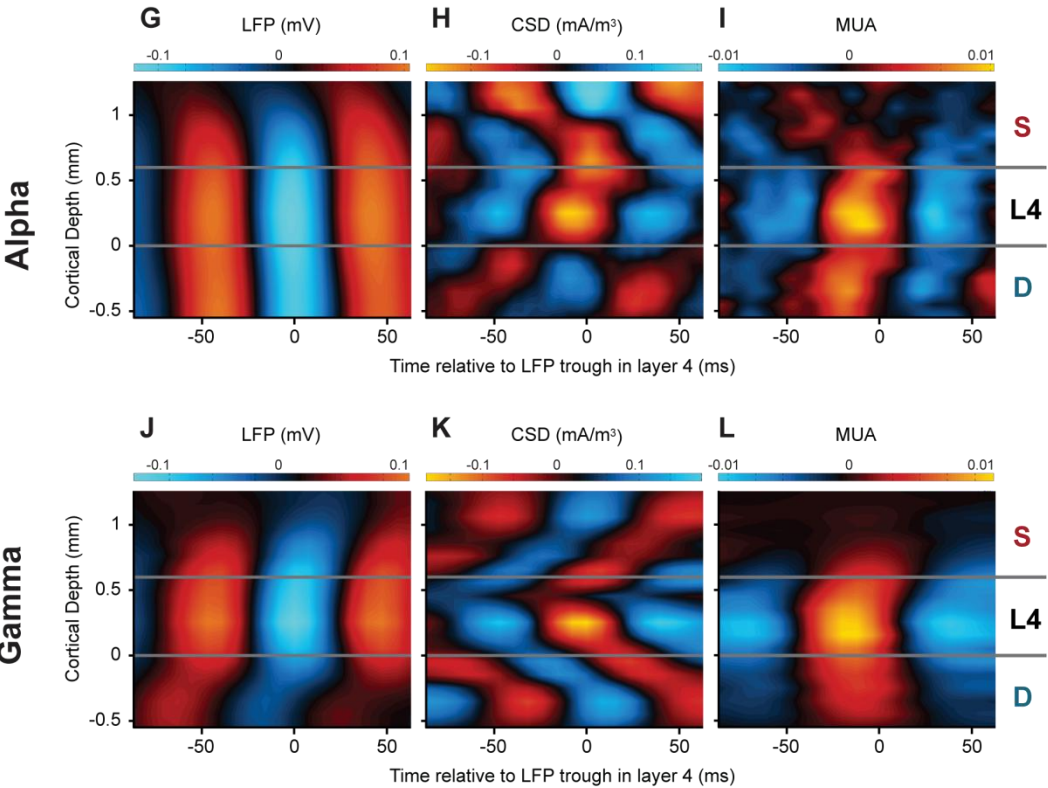


Fig. S11. Laminar profile of cortical oscillations for different task conditions. (A-C) Laminar profile of cortical oscillations if the figure fell in the neurons' RF. (A) Laminar profile of the LFP (mV) relative to the alpha troughs in a window from 150-300ms after stimulus onset, averaged across 24 penetrations. Negative potentials are shown in blue, positive potentials in red. (B) Average laminar profile of the CSD (mA/m^3) relative to LFP troughs in layer 4 for the alpha rhythm. Current sinks are shown in red, sources in blue. (C) MUA aligned to the LFP troughs in layer 4. Red colors show MUA that is higher than the average and blue colors MUA lower than the average. (D-F) Same analysis as in A-C, but now the data was aligned to the troughs of the gamma rhythm (55-65Hz) in layer 4. (G-L) Same analysis as in A-F but for the catch trials in a late 300ms time window (400-700ms after stimulus onset).

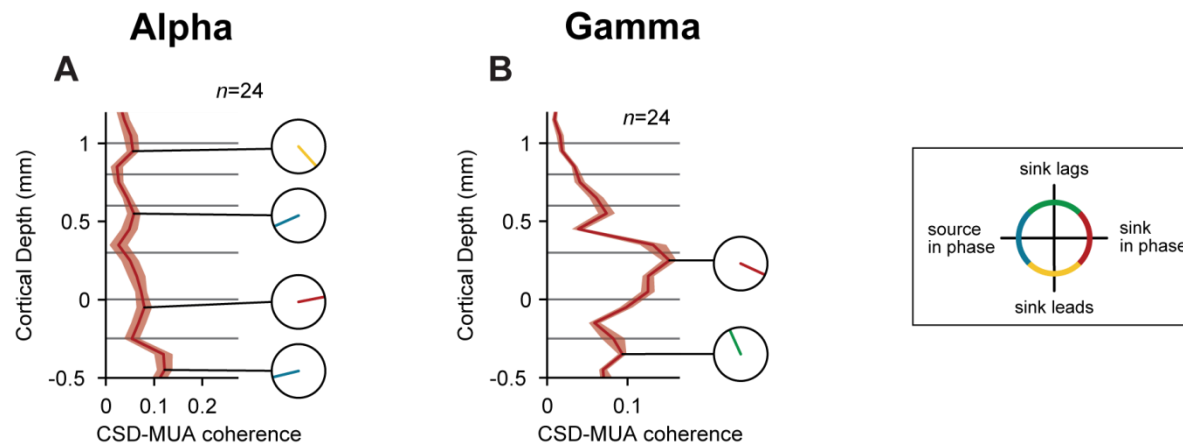


Fig. S12. Laminar profile of CSD-MUA coherence and phase for the figure condition. (A) Laminar profile of coherence between the layer-specific CSD and the MUA averaged across all layers, for the alpha band. There were four peaks in the coherence and the small circles show the phase of the CSD relative to the MUA. (B) Laminar profile of the CSD-MUA coherence in the gamma frequency range.

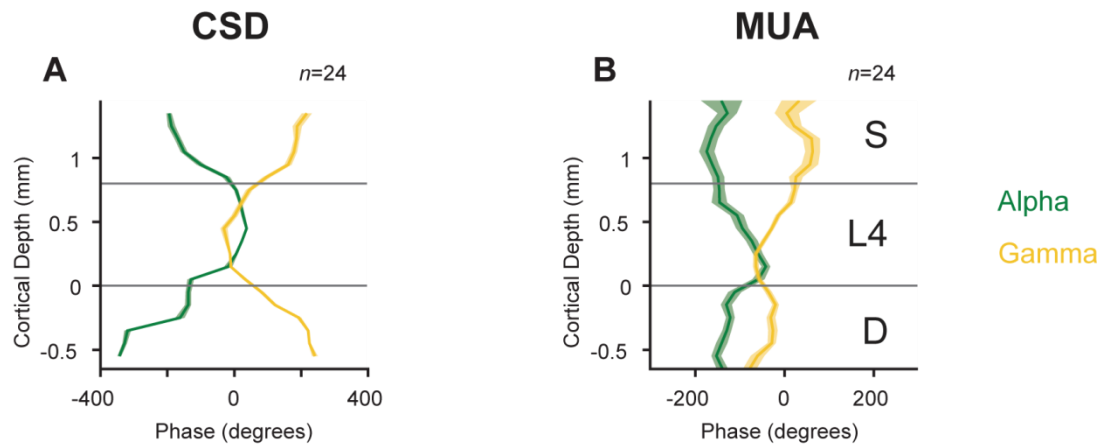


Fig. S13. Phase differences of the CSD and MUA in the different layers relative to the LFP in layer 4. (A) We used the LFP in layer 4 as reference signal and computed the phase of the CSD in the different layers for the alpha (green line) and gamma rhythm (yellow line). (B) Phase of the MUA in the different layers relative to the LFP in layer 4 for alpha and gamma activity. Shaded areas show s.e.m. ($n=24$ penetrations).

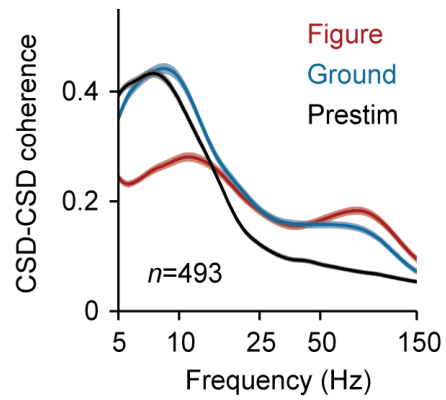


Fig. S14. Coherence of the CSD between sites on the laminar probe with a distance of 200 μ m in the figure (red trace) and background condition (blue trace) during the modulation period, and the pre-stimulus period (black trace). Shaded areas show s.e.m. in all plots (n=493 recording sites).

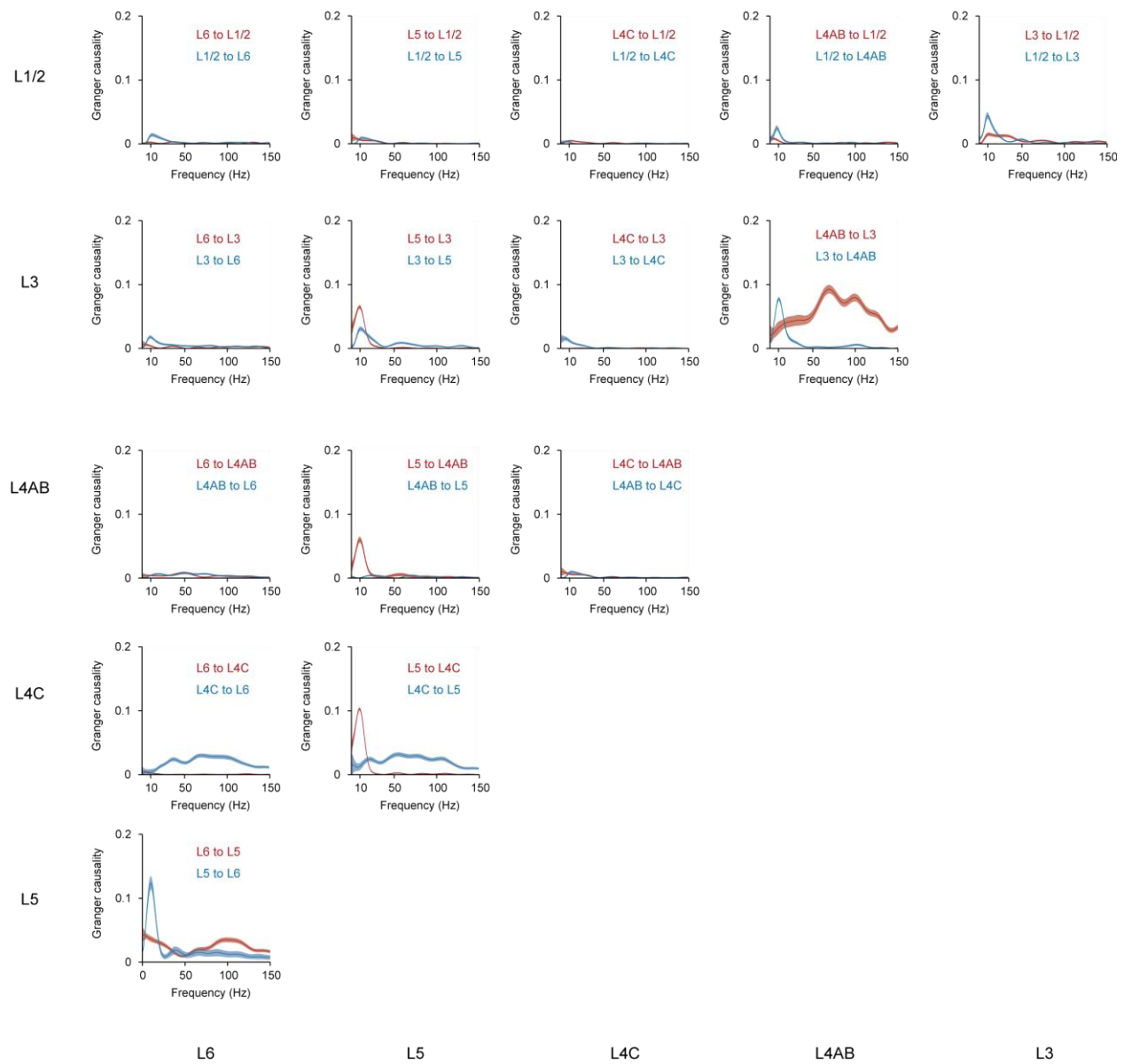


Fig. S15. Multivariate Granger causality of the CSD between the different layers in V1. Red lines indicate Granger causality in the upward direction (towards the pia), blue lines in the downward direction (towards the white matter). Shaded areas show s.e.m. (n=24 penetrations).

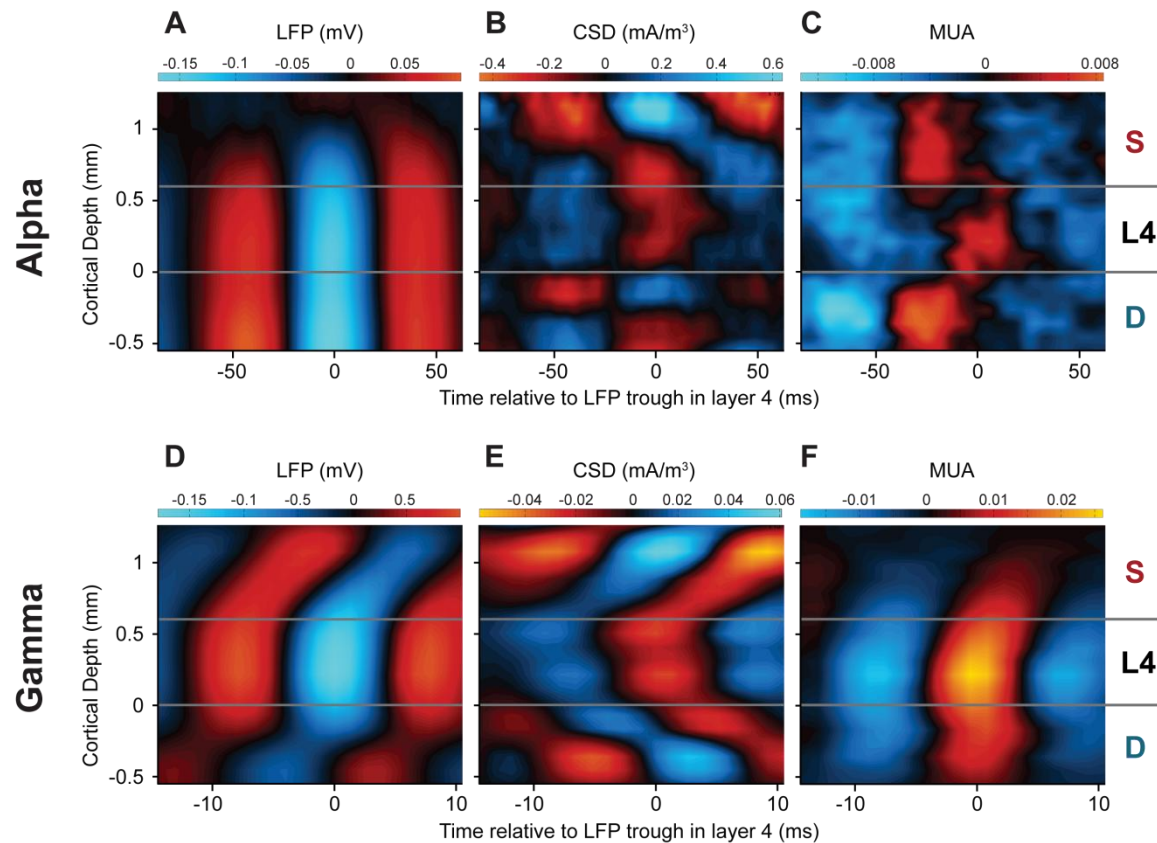


Fig. S16. Laminar profile of cortical oscillations in the curve tracing task. (A) Laminar profile of the LFP (mV) relative to the alpha troughs, in a window from 200-750ms after stimulus onset with the RF on the distractor curve, averaged across 16 penetrations. Negative potentials are shown in blue, positive potentials in red. (B) Average laminar profile of the CSD (mA/m^3) relative to LFP troughs in layer 4 for the alpha rhythm. Current sinks are shown in red, sources in blue. (C) MUA aligned to the LFP troughs in layer 4. Red colors show MUA that is higher than the average and blue colors MUA lower than the average. (D-F) Same analysis as in A-C, but now the data was aligned to the troughs of the gamma rhythm (55-65Hz) in layer 4.

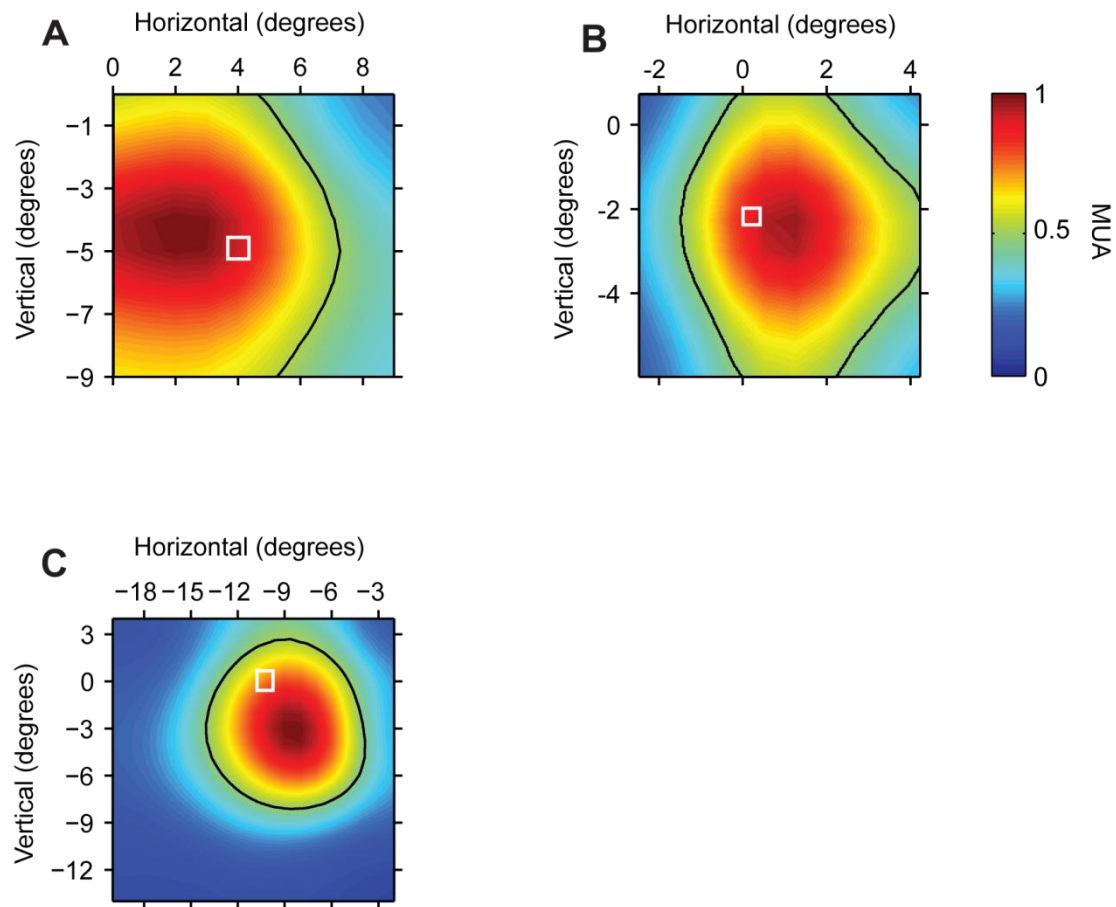


Fig. S17. RFs of recording sites in V1 (white squares) and V4 (color plots) in the three monkeys.

Black line indicates region beyond which the V4 response falls below 50% of the maximum.

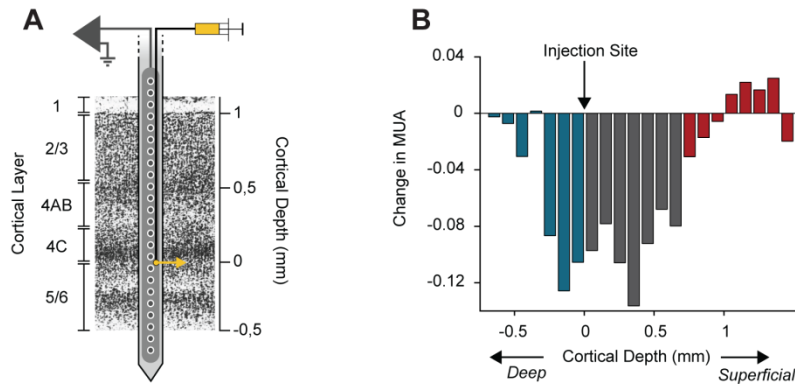


Fig. S18. Spread of pharmacological substances. (A) Drugs were injected through a fluid line. The yellow arrow indicates the approximate location of the fluid line exit. (B) An example recording where CNQX was injected at the boundary between layer 4c and layer 5 to measure the diffusion of the drug. The bars indicate the change in the average MUA response evoked by the appearance of the visual stimulus at each recording site (between 0-200ms after stimulus onset in normalized units) after injection of the drug. It can be seen that the drug diffuses from the injection site with a slight preference to spread towards the superficial sites, back along the shaft of the electrode. The maximum extent of the drug effect is ~1.5mm. The colors of the bars represent the different cortical layers, deep in blue, layer 4 in grey and superficial in red.

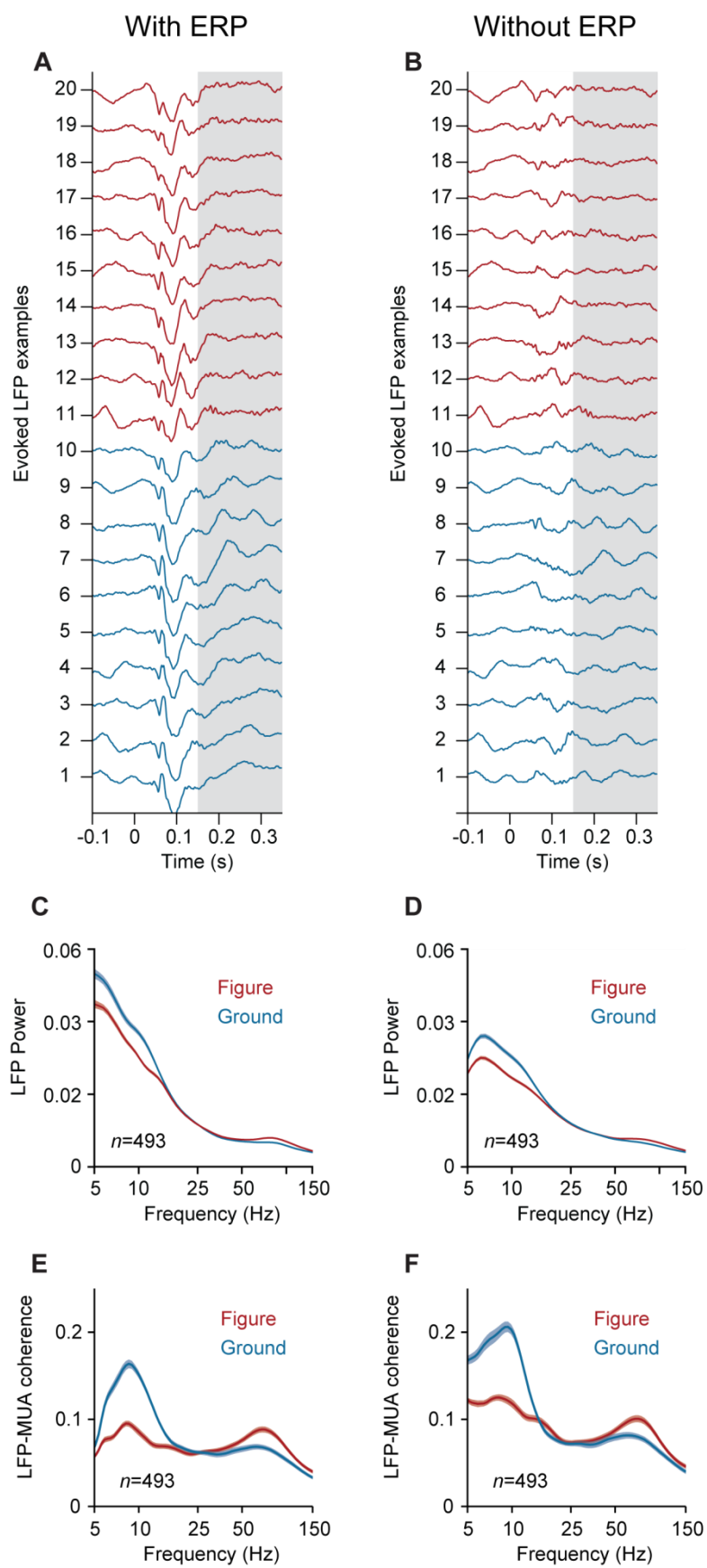


Fig. S19. Neuronal activity in single trials of the texture segregation task and the effect of subtracting the evoked potential. (A) LFP responses in successive trials of an example recording session without subtraction of the mean LFP response. Trials of the figure condition are shown in red and trials of the ground condition in blue. (B) LFP in the same trials after subtraction of the evoked potential. Grey area highlights the analysis window for frequency analysis (150-350ms after stimulus onset). (C,D) The average LFP power spectrum across all penetrations before (C) and after subtraction of the evoked potential (D). (E,F) The average LFP-MUA coherence spectrum across all penetrations before (E) and after subtraction of the LFP evoked potential (F). Red, figure condition; blue, ground condition. Shaded areas show s.e.m. ($n=493$ recording sites).

References

1. Supèr, H. & Roelfsema, P. R. (2005) Chronic multi-unit recordings in behaving animals: advantages and limitations. *Prog. Brain Res.* **147**, 263-282.
2. Logothetis, N. K., Pauls, J., Augath, M., & Oeltermann, A. (2001) Neurophysiological investigation of the basis of the fMRI signal. *Nature* **412**, 150-157.
3. Xing, D., Yeh, C.-I., & Shapley, R. M. (2009) Spatial spread of the local field potential and its laminar variation in visual cortex. *J. Neurosci.* **29**, 11540-11549.
4. Logothetis, N. K. (2002) The neural basis of the blood-oxygen-level-dependent functional magnetic resonance imaging signal. *Philos. Trans. R. Soc. Lond B Biol. Sci.* **357**, 1003-1037.
5. Zeitler, M., Fries, P., & Gielen, S. (2006) Assessing neuronal coherence with single-unit, multi-unit, and local field potentials. *Neural Comput.* **18**, 2256-2281.
6. Mitzdorf, U. (1985) Current source-density method and application in cat cerebral cortex: investigation of evoked potentials and EEG phenomena. *Physiol. Rev.* **65**, 37-100.
7. Logothetis, N. K., Kayser, C., & Oeltermann, A. (2007) In vivo measurement of cortical impedance spectrum in monkeys: implications for signal propagation. *Neuron* **55**, 809-823.
8. Mitzdorf, U. & Singer, W. (1979) Excitatory synaptic ensemble properties in the visual cortex of the macaque monkey: a current source density analysis of electrically evoked potentials. *J. Comp Neurol.* **187**, 71-83.
9. Buzsaki, G., Anastassiou, C. A., & Koch, C. (2012) The origin of extracellular fields and currents--EEG, ECoG, LFP and spikes. *Nat. Rev. Neurosci.* **13**, 407-420.
10. Schroeder, C. E., Tenke, C. E., Givre, S. J., Arezzo, J. C., & Vaughan, H. G., Jr. (1991) Striate cortical contribution to the surface-recorded pattern-reversal VEP in the alert monkey. *Vision Res.* **31**, 1143-1157.
11. Lund, J. S. (1973) Organization of neurons in the visual cortex, area 17, of the monkey (macaca mulatta). *J. Comp. Neurol.* **147**, 455-495.
12. O'Kusky, J. & Colonnier, M. (1982) A laminar analysis of the number of neurons, glia, and synapses in the adult cortex (area 17) of adult macaque monkeys. *J. Comp Neurol.* **210**, 278-290.
13. Nelson, M. J., Pouget, P., Nilsen, E. A., Patten, C. D., & Schall, J. D. (2008) Review of signal distortion through metal microelectrode recording circuits and filters. *J. Neurosci. Methods* **169**, 141-157.
14. Bour, L. J., Van Gisbergen, J. A. M., Bruijns, J., & Ottes, F. P. (1984) The double magnetic induction method for measuring eye movements: results in monkeys and man. *IEEE Trans. Biomed. Eng.* **31**, 419-427.
15. Kato, H., Bishop, P. O., & Orban, G. A. (1978) Hypercomplex and simple/complex cell classifications in cat striate cortex. *J. Neurophysiol.* **41**, 1072-1095.

16. Motter, B. C. (2009) Central V4 receptive fields are scaled by the V1 cortical magnification and correspond to a constant-sized sampling of the V1 surface. *J. Neurosci.* **29**, 5749-5757.
17. van der Togt, C., Kalitzin, S., Spekreijse, H., Lamme, V. A., & Super, H. (2006) Synchrony dynamics in monkey V1 predict success in visual detection. *Cereb. Cortex* **16**, 136-148.
18. Bendat, J. S. & Piersol, A. G. (2000) *Random data analysis and measurement procedures*. (John Wiley & Sons, Inc..
19. Fries, P., Womelsdorf, T., Oostenveld, R., & Desimone, R. (2008) The effects of visual stimulation and selective visual attention on rhythmic neuronal synchronization in macaque area V4. *J. Neurosci.* **28**, 4823-4835.
20. Berens, P. (2009) CircStat: A Matlab Toolbox for Circular Statistics. *Journal of Statistical Software* **31**, 1-21.
21. Steriade, M. & Amzica, F. (1996) Intracortical and corticothalamic coherence of fast spontaneous oscillations. *Proc. Natl. Acad. Sci. USA* **93**, 2533-2538.
22. Destexhe, A., Contreras, D., & Steriade, M. (1999) Spatiotemporal analysis of local field potentials and unit discharges in cat cerebral cortex during natural wake and sleep states. *J. Neurosci.* **19**, 4595-4608.
23. Barnett, L. & Seth, A. K. (2014) The MVGC multivariate Granger causality toolbox: a new approach to Granger-causal inference. *J. Neurosci. Methods* **223**, 50-68.
24. Bollimunta, A., Chen, Y., Schroeder, C. E., & Ding, M. (2008) Neuronal mechanisms of cortical alpha oscillations in awake-behaving macaques. *J. Neurosci.* **28**, 9976-9988.
25. Bollimunta, A., Mo, J., Schroeder, C. E., & Ding, M. (2011) Neuronal mechanisms and attentional modulation of corticothalamic alpha oscillations. *J. Neurosci.* **31**, 4935-4943.
26. Nieuwenhuys, R., ten Donkelaar, H. J., & Nicholson, C. (1998) *The central nervous system of vertebrates* (Springer-Verlag.
27. Krieg, W. J. S. (1975) *Interpretive atlas of the monkey's brain* (Brain Books, Evanston, Ill).